Laser ultrasonics for defect detection and residual stress measurement of friction stir welds

Lévesque, Daniel; Dubourg, Laurent; Blouin, Alain

Publisher's version / Version de l'éditeur:
https://doi.org/10.1080/10589759.2011.573551
Nondestructive Testing and Evaluation, 26, 3-4, pp. 319-333, 2011-09-30

Nondestructive evaluation of friction stir welds using laser ultrasonics

Daniel Lévesque[1], Laurent Dubourg[2*] and Alain Blouin[1]

[1] Industrial Materials Institute, National Research Council of Canada
75 de Mortagne Blvd., Boucherville, Québec, J4B 6Y4 Canada;
Corresponding author, Tel: 514-641-5240, Fax: 514-641-5106
daniel.levesque@cnrc-nrc.gc.ca

[2] Institute for Aerospace Research, National Research Council Canada,
Montreal, Quebec, H3S 2S4 Canada
[*] Now at Institut Maupertuis, Contour Antoine de St-Exupéry,
Campus de Ker Lann 35170 Bruz – France

Abstract
The laser-ultrasonic technique is investigated for defect detection and sizing as well as residual stress measurement in welds obtained by friction stir welding. When combined with the Fourier domain synthetic aperture focusing technique, very good performances are achieved for detecting lack of penetration in butt joints, the detection limit coinciding with the conditions of reduced mechanical properties. Also, the detection of kissing bonds seems to be possible in lap joints when probing with ultrasonic frequencies up to 200 MHz. Residual stresses induced by the FSW process can also be probed by laser ultrasonics. The method is based on monitoring the velocity change of the laser generated surface skimming longitudinal wave, propagating just below the surface and being found much more sensitive to stress. The residual stress profile measured across the weld line is in good agreement with results from a finite element model and from strain gauge measurements.

Keywords: Friction stir welding, laser ultrasonics, synthetic aperture focusing technique, kissing bond, residual stress, surface skimming longitudinal wave

1. Introduction

Friction stir welding (FSW) is a solid-state, environmentally friendly joining process that produces high strength and good finish welds. As shown in Figure 1, FSW uses a specially shaped rotating tool consisting of a pin and a shoulder to produce the weld. The motion of the welding tool on the metal plate, usually aluminum, generates frictional heat that creates a plasticized region around the immersed portion of the tool to produce lap or butt joints. The advancing and retreating sides of the weld correspond to locations where the maximum and minimum relative velocities between the rotating tool and the work piece are observed. During the last few years, FSW has been gaining acceptance and has found various applications in aerospace, automotive and naval industries. For example, high strength 2xxx and 7xxx series aluminium alloys can be easily joined using FSW, while these alloys are often considered very difficult to weld using conventional welding techniques [1, 2]. In the aerospace industry, stronger and lighter friction stir welded joints are excellent candidates for replacing bonded and riveted joints in the manufacture of large fuselage and other components [3, 4].

Validation of weld quality made by different methods is frequently done by both destructive and nondestructive testing. For FSW however, nondestructive inspection is not yet clearly established, especially due to specific defects and their random orientation within the weld. Typical FSW defects are lack of penetration of the tool, wormholes and vertical kissing bonds in butt joints, and hooking, wormholes and horizontal kissing bonds in lap joints [5]. Kissing bonds originate from the remnants of trapped oxide layers resulting in inferior mechanical properties in the weld nugget [6]. They are known as the most challenging problem for inspection of FSW joints. For the manufacturing of large size and complex structures, reliable methods have to be found to nondestructively evaluate the integrity of the welds produced by FSW. From the literature, only a few results have been reported to date for the detection of the defects described above [7-9]. Both ultrasonic-based methods and eddy current techniques have been found promising for this purpose; however, their actual performance for detecting these critical defects, particularly for kissing bonds is still uncertain. Moreover, little data exists on the relationship between nondestructive testing information and the quality of the weld in terms of its mechanical performance.

Figure 1 near here

In addition to defects, distortion in thin section structures caused by buckling due to thermal residual stresses usually occurs. This weld distortion can result in poor dimensional control and structural integrity. Techniques such as reduction of weld size, design modifications and thermal tensioning can be used to minimize residual stresses and related buckling [10]. There is a need to evaluate in a nondestructive manner the level of residual stresses to support such techniques. However, very few experimental methods are available for reliable quantitative evaluation of the residual stresses on large welded structures. Measurements of residual stresses in FSW were recently reported using a scanning acoustic microscope [11, 12]. Ultrasonic Rayleigh surface wave and through-thickness longitudinal wave show a small velocity difference between the parent material and the material in the welded region which was attributed to thermal residual stresses induced by the FSW process.

In this paper, laser ultrasonics, a non contact method using lasers for the generation and detection of ultrasound [13, 14], is considered for both defect detection and residual stress measurement, ultimately on-line during welding. For FSW defects, data acquisition across the weld line is made and numerical focusing is performed using the Fourier domain Synthetic Aperture Focusing Technique (F-SAFT) [15]. Lap and butt joints are examined along with metallographic analysis and validation by destructive mechanical testing. For residual stress, the method is based on monitoring the small velocity change produced by the stress of the laser generated surface skimming longitudinal wave (LSSLW or P-wave). This wave propagates just below the surface and is found much more sensitive to stress than Rayleigh wave (SAW) [16]. The residual stress profile measured across the weld line is compared to results from numerical simulations and strain gauge measurements. Also, an investigation is made about microstructural changes that could affect the measurement.

2. FSW defect detection

2.1 Laser-ultrasonic setup for defect detection

The approach to detect different types of flaws in FSW is illustrated in Figure 2. Using F-SAFT, the generation and detection spots overlap at the surface of the part. The generation of ultrasound is performed in the slight ablation regime with a 35 ps duration pulse of a Nd:YAG laser in its 3rd harmonic with a spot size of about 50 μm. The detection uses a long pulse Nd:YAG laser in conjunction with a photorefractive interferometer for demodulation. Frequencies up to 220 MHz are generated and detected in the weld region. A 2-D scan is performed for data acquisition with a step size of 0.1 mm. The scans are performed after the removal by milling of any welding debris that could interfere with the recorded signal. For the numerical focusing, an algorithm in the Fourier domain is used for time-efficient reconstruction [15]. One advantage of laser ultrasonics is being able to produce small spots on the surface which allows numerical focusing at shallow depths as in the joining of thin plates.

Figure 2 near here

2.2 Inspection of lap joints

All welds were produced on a MTS I-STIR FSW machine. Lap joint samples using FSW for aerospace application, consisting of a 1.5 mm thick plate of AA7075-T6 on top of a 2.5 mm thick plate of AA2024-T3, were performed with different pin shapes and welding parameters in order to create different defects. The standard tool with a scrolled shoulder (19 mm diameter) and a pin (6.3 mm diameter pin) was used. Figure 3 shows an F-SAFT image of a cross-section (or B-scan) and the corresponding metallography of a lap joint, with inspection from the far side of the tool. The presence of hooking in the advancing side near the interface is clearly visible. F-SAFT reconstruction is found very useful for the identification of hooking defects by properly reducing the size of an indication having a parabolic shape. A wormhole is also observed and occurs when the ratio between the welding speed and the tool rotation speed is too high or too low [17]. More importantly, a kissing bond is detected as a slight reflection along the interface, in addition to that from the weld surface.

Figure 3 near here

This capability was further investigated on a sample with pre-oxidation of the surfaces. The oxide layer was produced on the sheets before welding by using sulphuric anodization. Aluminum sheets that had been surface activated with Durmax alumina, were pickled by plunging them in sodium hydroxide solution at 100 g/l, and rinsed. Afterwards, they were plunged into a dip of sulphuric acid (H_2SO_4) at a concentration between 180 g/l and 200 g/l. The acid bath was stirred with a magnetic stirrer and maintained at a temperature of 20°C. A current density of 1.5 A/dm^2 was imposed to produce the anodization. The imposed current was about 10 A because of the dimensions of the plate (35 cm x 10 cm) and optimal lap joining parameters were used for welding these plates (speed: 900 mm/min, spindle: 700 rpm, force: 18 kN, double pass). Except for two voids, all welds were of high quality, with one weld produced per anodisation condition. In Figure 4, a dark line which could be an oxide layer can be observed at the remnant interface of the sample which has been anodized during 10 min. It is observed as dark particles dispatched in the weld.

The SAFT approach was used to detect this oxide layer. As shown in Figure 5, a kissing bond present in the weld is clearly detected again from the far side as a slight reflection along the interface for an oxide layer 8 μm thick. Bending tests revealed that the oxide layer may impact on the weld quality by reducing the mechanical properties if the oxide layer is thicker that 2 μm. Therefore, such experiment proved that the sheets must be cleaned before welding to avoid this defect.

Figure 4 near here

Figure 5 near here

2.3 Inspection of butt joints

Samples were welded using FSW in butt configuration. A first sample was prepared with 2-mm thick AA7075-T6 sheets with a tool composed of a concave shoulder (diameter of 10 mm) and a threaded cylindrical pin (diameter of 3 mm). The pin length was purposely made too short (1.2-mm long) to produce a lack of penetration (LOP). Figure 6 shows an F-SAFT image and the corresponding metallography of a cross-section of the butt joint with a constant LOP. Measurements were made on the tool side to detect the LOP on the opposite side. The LOP is well observed and appears as a lack of signal of the longitudinal wave near the bottom surface. From metallography, the LOP shown has a width of about 10 μm and a depth of 0.6 mm. The detection of a 0.3 mm deep LOP in a similar specimen was also observed. However, the quantitative estimation of the depth appears difficult, a situation similar to that found in a previous work for crack detection [18]. Also, the shear wave, usually generated in laser-ultrasonics, was too weak in this Al alloy and not practical for SAFT reconstruction.

Figure 6 near here

A comparison between the detection limit and the mechanical performance was investigated. For this purpose, a second butt joint was prepared using 2.5-mm thick AA2024-O sheets with a tool composed of a scrolled shoulder (diameter of 19 mm) and a threaded cylindrical pin (diameter of 6.3 mm). For this experiment, the pin penetration was progressively increased from 1.2 mm to 2.5 mm during welding along the 355-mm in length joint. This operation introduced a variable weld depth and, consequently, a gradual LOP on the back-side of the weld. Metallographic examination at several locations revealed a LOP for a penetration of the rotating tool (shoulder and pin) lower than 2.2 mm from the top surface. Notice that to produce a good weld, the pin does not have to touch the bottom surface of the plate because of the stirring action. The inspection of regions of dimensions 10 mm x 10 mm was performed along the weld at regular intervals. Figure 7 shows the F-SAFT images of the bottom surface at different locations, with the pin penetration indicated for each image. Indications of LOP along the weld are well observed for pin penetrations less than 2.2 mm, starting from a continuous line and finishing with an irregular trace. The irregular appearance of a LOP implies that many cross-sectional views are required for weld assessment by metallography. Bending tests were also performed on different portions of this sample. No failure was observed for pin penetration larger than 2.1 mm. This is in good agreement with the F-SAFT results as well as with those from metallography.

Figure 7 near here

2.4 Inspection of T-joints

For the assembly of T-joints, a special clamping device was used on the MTS I-STIR FSW machine. Several T-joints made of 4-mm thick 6013-T6 top plates were welded to 2.3-mm thick 2024-T3 plates. The welding parameters were optimized to obtain welds free of defects from visual inspection. Using a large tool with a pin diameter of 5 mm and a shoulder of 13 mm, a rotational speed of 1000 rpm and a welding speed of 150 mm/min, apparent good welds were obtained as shown in Figure 8. However, a clear defect was observed by metallography as shown in Figure 9a. This defect was located at the retreating side and was about 400 μm in size. Moreover, a small hooking (about 200 μm) was observed at the advancing side in Figure 9b.

Figure 10 shows two C-scans after F-SAFT reconstruction at the depths indicated in the B-scan for the T-joint above obtained with optimized process parameters. The C-scan at the interface level shows no defect; therefore, a good stirring of the materials is assumed. However, the C-scan at 0.6 mm below the interface level (bottom left of Figure 10) shows a continuous indication on the retreating side (RS) corresponding to a point in the B-scan of Figure 10. This seems to be in line with the defect observed by metallography. However, the small hooking observed in the metallography on the advancing side is not detected by laser ultrasonics.

Figure 8 near here

Figure 9 near here

Figure 10 near here

Figure 11 shows two C-scans and a B-scan for another T-joint performed with different welding process parameters. The C-scan at the interface level shows indications associated with a large wormhole along the weld line, a feature that is also observed in the B-scan in the region slightly above the interface. Also, the C-scan at 0.6 mm below the interface level shows a continuous line indication on the advancing side (AS) which corresponds to a point in the B-scan (Figure 11b). This situation is different than for the previous T-joint which had a defect on the retreating side (RS).

Figure 11 near here

3. Residual stress measurement

3.1 Test sample and numerical analysis

Regarding residual stress analysis, weldments made of 2.3-mm thick AA2024-T3 sheets were produced in butt configuration using a standard FSW tool (cylindrical threaded pin of 6.3-mm diameter and a concave shoulder of 12.7-mm diameter). A travel speed of 6 mm/s and a spindle rotating speed of 1000 rpm were used to weld 300 x 150 mm^2 sheets. The weld axis was perpendicular to the rolling direction of the parent plate. The above FSW parameters resulted in sound and defect-free welds. During welding the test coupon was clamped tightly on a thick steel plate. This portable clamping anvil avoided the deformation of the test coupon during and after welding thereby retaining the residual stresses inside the material. Measurements of the residual stresses were carried out using the destructive technique of hole drilling. Two strain gauges were placed on each side of the zone to be drilled. The local strain ε due to the drilling is measured and the longitudinal stress is calculated using the relation:

$$\sigma_{\max} = -\left[\frac{1}{2a(1+\upsilon)} + \frac{1}{2b}\right] E\varepsilon \qquad (1)$$

where the coefficients a, b depend on the hole diameter and the distance between the two gauges, E = 73.1 GPa and υ = 0.33 are the Young's modulus and the Poisson's ratio for the AA2024-T3. After metallurgical preparation, Vickers microhardness was measured through the weld cross section over a length of 30 mm and at respectively 0.5, 1 and 1.5 mm from the upper surface. A sampling step of 500 μm and a load of 300 g applied during 15 sec were employed.

The FSW process performed on the test coupon was simulated by a 3D finite element model (FEM) using the LS-Dyna package. For simplicity, the FSW tool was modeled as a heat source moving along the weld seam without material stirring. This is a reasonable assumption as the formation of residual stresses in FSW is mainly dominated by the heat input and the thermal expansion [19]. The heat flow and the generation of residual stresses during FSW were simulated using sequential coupled finite element model. The first step was a transient heat flow analysis that calculates the temperature distribution in the coupon

during welding (t = 25 s) and cooling cycles (t = 100 s). The second step was the mechanical simulation, using as input the thermal history obtained in the first step. The weld coupon and the backing anvil were modeled as a 3D half model, the symmetry being the weld centre line. For the thermal analysis, the boundary condition was the heat generation below the tool shoulder, with a heat flux of $11x10^6$ W/m^2 corresponding to the above FSW parameters. The surface temperature of the sample was low; consequently, the radiation heat and convection losses were negligible. For the mechanical analysis, the tool shoulder and the backing anvil were treated as rigid contact surfaces. The longitudinal edges of the coupon were restrained to simulate the clamping fixture applied during and after welding.

Figure 12 shows the temperature profile across the weld line when the maximum temperature is reached as well as the stress profiles after welding. The z stress is along the weld axis and the x stress is across the weld. The maximum temperature is about 300^{o}C at 8 mm from the weld center and progressively decreases. The calculated temperature profile is in agreement with results obtained from thermocouple measurements. With such temperature gradients, the z stress after welding is about 250 MPa (tension) near the weld center and rapidly decreases to -25 MPa (compression) at about 8 mm. The x stress progressively decreases from 150 MPa to about 75 MPa. Both the z and x stresses cause the distortion as shown in Figure 1. Another important result from the simulations is that stresses are almost constant through the thickness of the sheet, except near the weld center, therefore making residual stress measurement much easier. The phenomenon may be explained by the relative thinness of the used aluminum coupons compared to the large size and power of the heat source. In this case, the thermal gradients are almost zero through the coupon thickness, resulting in constant stresses.

Figure 12 near here

3.2 Laser-ultrasonic setup for residual stress measurement

The laser-ultrasonic setup is presented in Figure 13. The same generation laser, detection laser and photorefractive interferometer are used, but with a separation between a line source and line detection. A laser line generation and line detection configuration was chosen to minimize wave spreading as well as microstructure noise, its use being similar to spatial averaging. The line dimension is about 6 mm long per 50 μm wide for the generation and 3 mm long per 50 μm wide for the detection. With this configuration, P-wave and SAW up to 30 MHz are generated and detected in aluminum. However, a bandpass filter was applied to all signals for velocity measurements at a center frequency of 10 MHz. A scanning system with a mirror and a translation table controls the source to receiver distance from 3 to 20 mm. The selection of an adequate distance is a trade-off between a sufficient SNR and time resolution associated with small velocity changes. Also, the sample is mounted on a translation table to get a stress profile. Neglecting the small coupling, the stress in a given direction is obtained by propagating the ultrasonic mode in that direction.

Figure 13 near here

For precise velocity measurement, cross-correlation of the signal associated to the P-wave or SAW arrival is performed with a reference signal obtained on an unstressed similar sample. The resulting time-of-flight (TOF) variation is related to the velocity variation by the simple formula $\Delta V/V = -\Delta t/t$, assuming no source-to-receiver distance variation. Since the P-wave is found much more sensitive to stress, σ, a compensation using the SAW can be made, for changes in path length or other effects, using the relation:

$$\frac{\Delta V}{V} = \frac{\Delta t_R}{t_R} - \frac{\Delta t_P}{t_P} \approx K_P \sigma \tag{1}$$

where the subscript denotes the wave mode (R: SAW or P: LSSLW). The acoustoelastic coefficient, K_P, can be obtained experimentally as calibration. A positive velocity (negative TOF) variation indicates a compressive (negative) residual stress.

The use of P-wave has been recently applied with some success for measuring compressive residual stresses induced after surface enhancement treatments to extend the fatigue life and prevent stress corrosion cracking [20, 21]. However, in this case, additional factors induced by the surface treatment such as surface roughness, crystallographic texture and dislocations were making the approach more challenging than with the FSW process.

3.3 Residual stress profile

Laser-ultrasonic measurements have been conducted on the test specimen clamped on a thick steel backing anvil. The TOF variations of the P-wave due to the z and x stresses as a function of the distance from the weld center were obtained, including SAW compensation for the other effects. For a more direct comparison, the coefficient K_P = -0.40 % / 100 MPa taken from [22] for aluminum was used. With this calibration, Figure 14 shows the profiles for both the z stress and x stress obtained from laser-ultrasonic measurements. The agreement with the calculated profiles in Figure 12b is very good, noting that the measurement range starts at about 7 mm from the weld centre line. One discrepancy however is the cross point of the z stress going from tensile to compressive stress at a position of 8 mm in the calculation, and 11 mm from laser-ultrasonic measurements.

Figure 14 near here

For comparison, stress measurements by the hole drilling technique using strain gauges were performed on three different coupons for the z stress only. Figure 15 shows the measured transverse profiles of the z stress on these specimens. Notice that the specimen used for laser-ultrasonic measurements is labeled sheet 3. While some erratic behavior is observed, there is a fairly good agreement between such results and those from the numerical analysis and laser ultrasonics. In the case of strain gauge measurements however, the cross point from tensile to compressive stress is at a position of about 20 mm, different than that of the calculation and laser ultrasonics. Recent results from the neutron diffraction technique showed that the cross point is closer to that of laser ultrasonics [23].

Figure 15 near here

3.4 Microstructural effect

While a good agreement is observed between the stress profile measured by laser ultrasonics and the other approaches, there is a need to evaluate the impact of heat involved in the FSW process that may change the microstructure and affect the laser-ultrasonic velocity measurements. In particular, one can suspect that part of the TOF profile in Figure 14 could be attributed to temperature variations across the weld line. Indeed, it is observed that the heat cycle in FSW joint causes a change of mechanical properties such as hardness up to 14 mm from the weld center, as shown in Figure 16.

Figure 16 near here

To investigate this aspect, several coupons from the same aluminum alloy in absence of stress and weld were heated at temperatures from 100 to 450^{o}C for 3 min and cooled down to room temperature. TOF measurements were performed on these coupons. Notice that in view of Figure 12a obtained from numerical simulations, the maximum temperature reached is less than 350^{o}C over the region of residual stress measurements on the FSW specimen.

Figure 17 shows the TOF variations on the small unstressed coupons heated at different temperatures for the P-wave and after correction with SAW. The TOF variations of the P-wave are small, within 0.03 %, for coupons heated at temperatures up to 250^{o}C where a sudden reproducible change occurs with a variation of about 0.25 %. This change may be attributed to the coalescence followed by the dissolution of the Guinier-Preston phases at higher temperatures in the 2024-T3 base metal [24]. However, the effect of such a transition on TOF is strongly reduced over the entire range up to 450^{o}C using the SAW correction. This is a fortunate situation where the two ultrasonic modes are affected in a similar manner and the correction cancels out the effect. Therefore, it seems reasonable to state that the transverse stress profile obtained by laser ultrasonics in Figure 14 is mostly due to residual stresses.

Figure 17 near here

4. Conclusions

The applicability of laser ultrasonics for both defect detection and residual stress measurement was demonstrated. Ultimately, the approach could allow fast scanning for weld assessment along the tool path. When combined with F-SAFT for defect detection, discontinuities such as wormholes, hooking and lack of penetration were clearly detected in the lap, butt or T-joint configuration. Moreover, the detection of kissing bonds could be possible in lap joints with frequencies up to 200 MHz. Lack of penetration in butt joints were shown to be irregular, which means that many cross-sectional views or bending tests are required. Also, the detection limit was found to coincide with the conditions of reduced mechanical properties.

Laser ultrasonics could also be used to measure residual stresses induced by the FSW process. The method is based on monitoring the small velocity change of the P-wave with

the SAW compensation for other effects. The residual stress profile measured across the weld line was in fairly good agreement with results from simulations and strain gauge measurements. However, the cross point from tensile to compressive stress was different for the different methods. This will be further investigated in future work with results from neutron diffraction technique on more specimens and the use of a more complete numerical model.

Acknowledgements

The authors would like to thank Martin Lord for their assistance in instrumentation for all aspects of this project, and Pascal Doran for his help in developing the finite element model of the FSW process.

References

[1] P. Cavaliere, R. Nobile, F.W. Panella, and A. Squillace, *Mechanical and microstructural behaviour of 2024–7075 aluminium alloy sheets joined by friction stir welding*, International Journal of Machine Tools and Manufacture 46 (2006), pp. 588-594.

[2] J. Q. Su, T. W. Nelson, R. Mishra, M. Mahoney, *Microstructural investigation of friction stir welded 7050-T651 aluminium,* Acta Materialia 51 (2003), pp. 713-729.

[3] B. Christner, J. Mc Coury, S. Higgins, *Development and testing of friction stir welding as a joining method for primary aircraft structure*, 4th International Symposium on Friction Stir Welding, Park City, UT, USA, 2003.

[4] W. J. Arbegast, A. K. Patnaik, *Process Parameter Development and Fixturing Issues for Friction Stir Welding of Aluminum Beam Assemblies,* AeroTech Congress & Exhibition, Grapevine, TX, USA, 2005.

[5] L. Dubourg, A. Merati and M. Jahazi, *Process Optimisation and Mechanical Properties of Friction Stir Lap Welds of 7075-T6 Stringers,* Materials and Design 31 (2010), pp. 3324-3330.

[6] Y.S. Sato, H. Takauchi, S.H.C. Park and H. Kokawa, *Characteristics of the kissing-bond in friction stir welded Al alloy 1050*, Mat. Sci. Eng. A 405, pp. 333-338 (2005).

[7] D. Kleiner and C.R. Bird, *Signal processing for quality assurance in friction stir welds*, Insight 46 (2004), pp. 85-87.

[8] A. Lamarre, *Eddy current arrays and ultrasonic phased-array technologies as reliable tools for FSW inspection*, Proc. of the 6th Intern. FSW Symposium, St-Sauveur (Qc), Canada, 2006.

[9] S. Iwaki, T. Okada, N. Eguchi, S. Tanaka, K. Namba and N. Oiwa, *Imperfections in friction stir welded zones and their precision non-destructive testing. Studies on characteristics of friction stir welded joints in structural thin aluminium alloys*, Welding Intern. 20 (2006), pp. 197-205.

[10] P. Michaleris and X. Sun, *Finite element analysis of thermal tensioning techniques mitigating weld buckling distortion*, Welding Journal 76 (1997), pp. 451-S – 457-S.

[11] R.W. Martin, S. Sathish and K.V. Jata, *Investigation of local elastic properties in friction stir welded Ti-6Al-4V using scanning acoustic microscopy*, Review of Progress in QNDE, Vol. 27, ed. by D.O. Thompson and D.E. Chimenti, AIP Conf. Proc., NY, pp. 1050-1057, 2008.

[12] S. Sathish, K.V. Jata, R.W. Martin and R. Reibel, *Challenges in detecting damage in the presence of microstructural inhomogenities in a friction stir welded aluminum alloy for reusable cryotanks*, Proc. of the SPIE, Health Monitoring and Smart Non-destructive Evaluation of Structural and Biological Systems, 6177, ed. by T. Kundu, pp. 617703-1 – 617703-9, 2006.

[13] C.B. Scruby and L.E. Drain, *Laser-Ultrasonics: Techniques and applications*, Adam Hilger, Bristol, UK, 1990.

[14] J.-P. Monchalin, *Laser-ultrasonics: from the laboratory to industry*, Review of Progress in Quantitative Nondestructive evaluation 23A, ed. by D.O. Thompson and D.E. Chimenti, AIP Conf. Proc., New York, pp. 3-31, 2004.

[15] D. Lévesque, A. Blouin, C. Néron and J.-P. Monchalin, *Performance of laser-ultrasonic F-SAFT imaging*, Ultrasonics 40 (2002), 1057-1063.

[16] C. Bescond, J.-P. Monchalin, D. Lévesque, A. Gilbert, R. Talbot and M. Ochiai, *Determination of residual stresses using laser-generated surface skimming longitudinal waves*, Proc. of the SPIE, Symp. on NDE for Health Monitoring and Diagnostics 5767, pp. 175-186, 2005.

[17] L. Dubourg, M. Jahazi, F.O. Gagnon, F. Nadeau, and L. St-Georges, *Process window optimization for FSW of thin and thick sheet Al alloys using statistical methods*, Proc. of the 6th Intern. FSW Symposium, St-Sauveur (Qc), Canada, 2006.

[18] M. Ochiai, D. Lévesque, R. Talbot, A. Blouin, A. Fukumoto, J.-P. Monchalin, *Detection and characterization of discontinuities in stainless steel by the laser ultrasonic synthetic aperture focusing technique,* Materials Evaluation (2004), pp. 450-459.

[19] D.G. Richards, P.B. Prangnell, P.J. Withers, S.W. Williams, A. Wescott, E. C. Oliver, *FE Modelling of Mechanical Tensioning for Controlling Residual Stresses in Friction Stir Welds*, Materials Science Forum, Proc. of Thermec 2006, Vancouver, Canada, Vols. 539-543, pp 4025-4030, 2007.

[20] C. Bescond, D. Lévesque, M. Lord, J.-P. Monchalin, S. Forgues, *Laser-generated surface skimming longitudinal wave measurement of residual stress in shot peened samples*, Review of Progress in QNDE, Vol. 25, ed. by D.O. Thompson and D.E. Chimenti, AIP Conf. Proc., NY, pp. 1426-1433, 2006.

[21] A. Moreau, C.S. Man, *Laser-ultrasonic measurements of residual stresses in a 7075-T651 aluminum sample surface-treated with low plasticity burnishing*, Review of Progress in QNDE, Vol. 25, ed. by D.O. Thompson and D.E. Chimenti, AIP Conf. Proc., NY, pp. 1434-1441, 2006.

[22] D.E. Bray and W. Tang, Subsurface stress evaluation in steel plates and bars using Lcr ultrasonic wave, Nuclear Eng. & Design 207 (2001), pp. 231-240.

[23] L. Dubourg, P. Doran, S. Larose, M.A. Gharghouri and M. Jahazi, *Prediction and measurements of thermal residual stresses in AA2024-T3 friction stir welds as a function of welding parameters*, Proc. of Thermec 2009, August 25-29, Berlin, Germany, 2009.

[24] J. R. Davis, *ASM Speciality Handbook, Aluminum and Aluminum Alloys*, ASM International, 1993.

Figure captions

Figure 1. Schematic of the FSW principle (butt joint).

Figure 2. Laser-ultrasonic setup for inspection of defect with F-SAFT.

Figure 3. Cross-section of a lap joint with many defects. a) F-SAFT image with inspection from the far side of the tool and b) corresponding metallography.

Figure 4. Oxide layer as a function of position into the weld.

Figure 5. F-SAFT image of oxidized FSW samples.

Figure 6. Cross-section of a butt joint with a lack of penetration. a) F-SAFT image with inspection from the tool side and b) corresponding metallography.

Figure 7. F-SAFT images of the bottom surface for different pin penetrations along the weld as indicated.

Figure 8. T-joint structure obtained with optimized parameters: a) cross-section metallography, b) picture of the part.

Figure 9. Metallography of a T-joint on the a) retreating side and b) advancing side.

Figure 10. C-scans (left) at the depths indicated in the B-scan (right) for a T-joint sample.

Figure 11. C-scans (left) at the depths indicated in the B-scan (right) for another T-joint sample.

Figure 12. Calculated transverse profile across the weld line of a) maximum temperature and b) residual stresses after welding from numerical simulation of the FSW process.

Figure 13. The laser-ultrasonic setup for residual stress measurement.

Figure 14. Transverse profile across the weld line of the z stress and x stress using laser ultrasonics.

Figure 15. Transverse profile of the z stress across the weld line with error bars on three specimens using strain gauges.

Figure 16. Cross section of the FSW weld and microhardness measurements at 1 mm from the upper surface.

Figure 17. TOF variation on small coupons unstressed, heated at different temperatures and measured at room temperature, a) for the P-wave and b) after correction with the SAW.

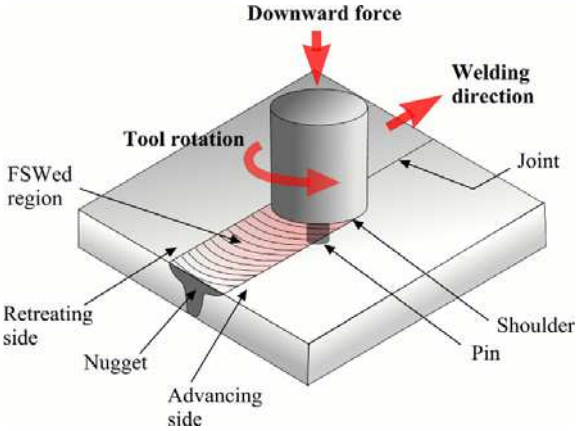

Figure 1. Schematic of the FSW principle (butt joint).

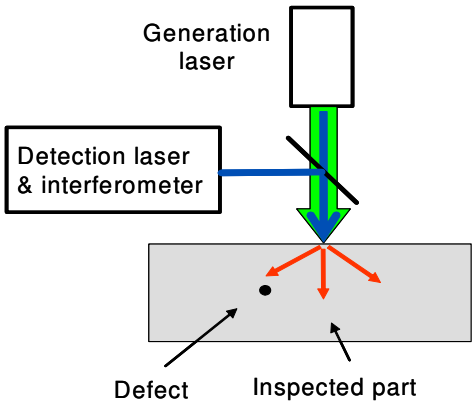

Figure 2. Laser-ultrasonic setup for inspection of defect with F-SAFT.

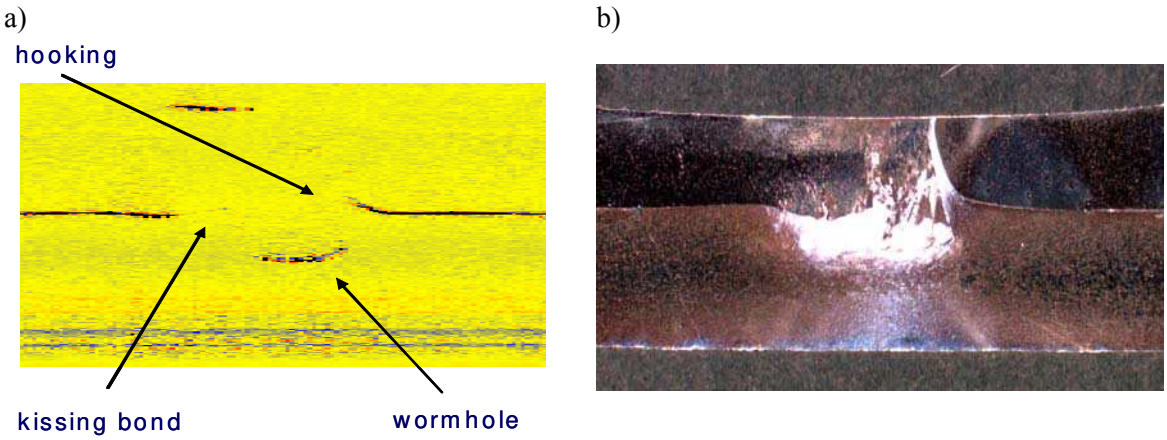

Figure 3. Cross-section of a lap joint with many defects. a) F-SAFT image with inspection from the far side of the tool and b) corresponding metallography.

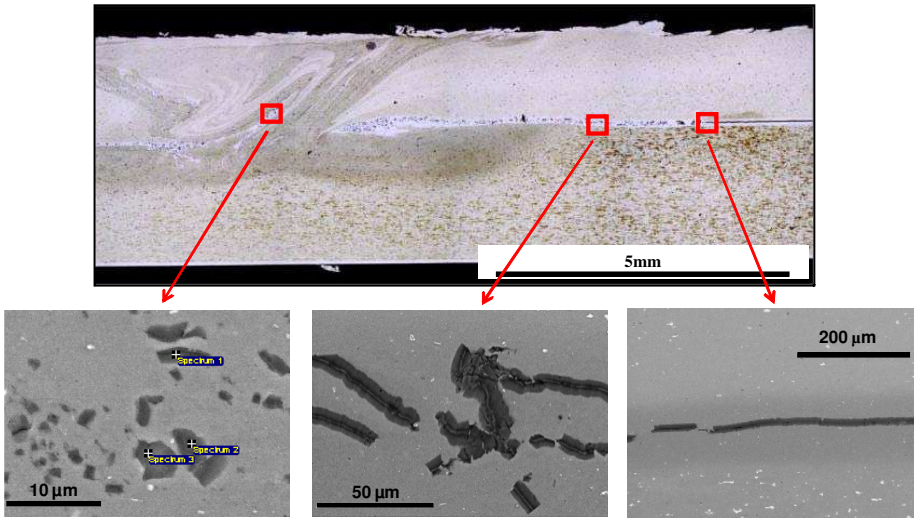

Figure 4. Oxide layer as a function of position into the weld.

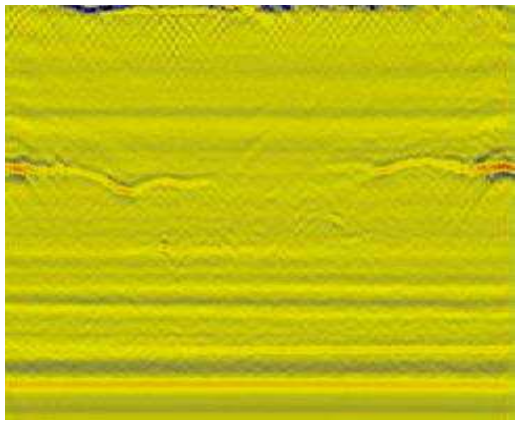

Figure 5. F-SAFT image of oxidized FSW samples.

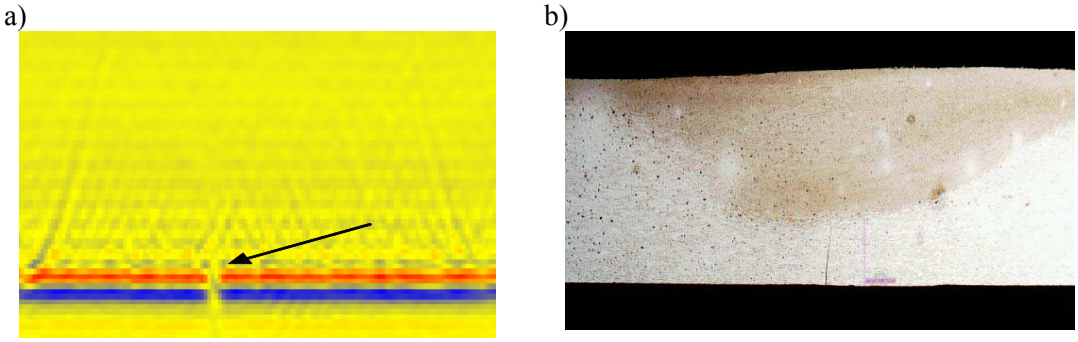

Figure 6. Cross-section of a butt joint with a lack of penetration. a) F-SAFT image with inspection from the tool side and b) corresponding metallography.

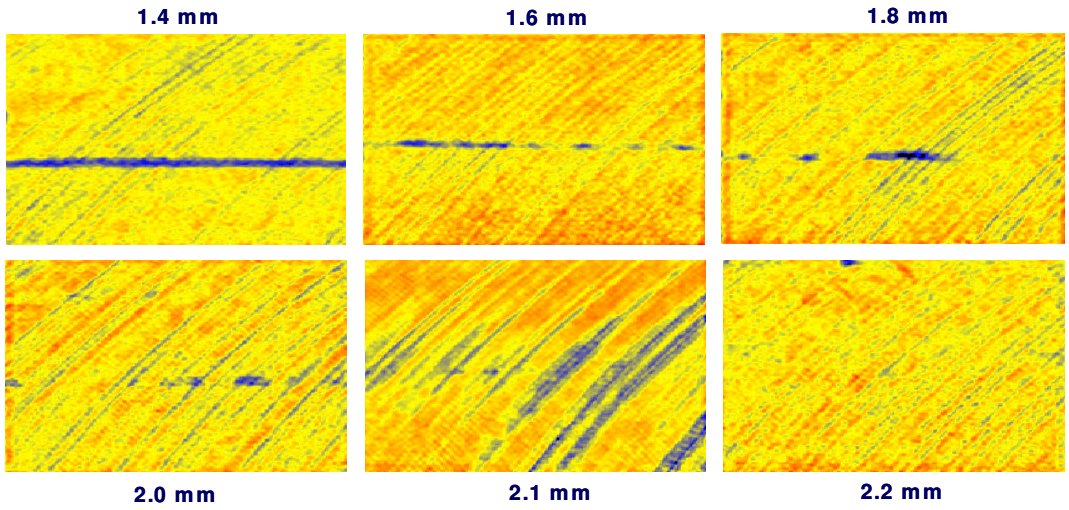

Figure 7. F-SAFT images of the bottom surface for different pin penetrations along the weld as indicated.

a) b)

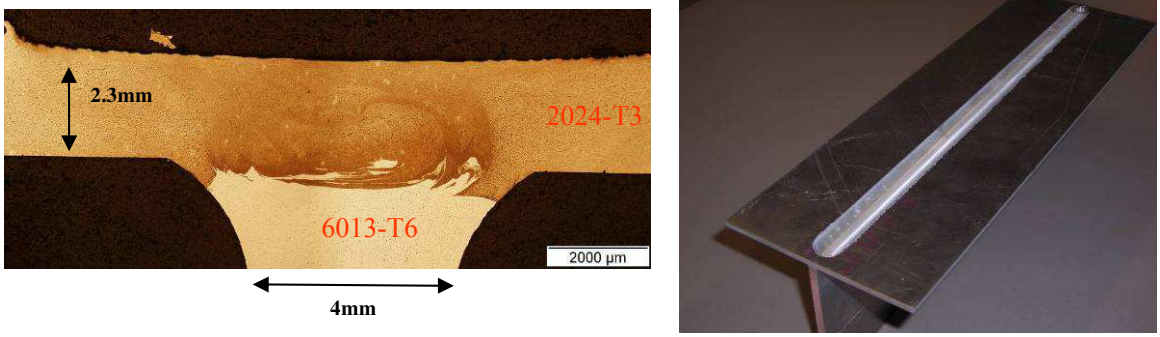

Figure 8. T-joint structure obtained with optimized parameters: a) cross-section metallography, b) picture of the part.

a) b)

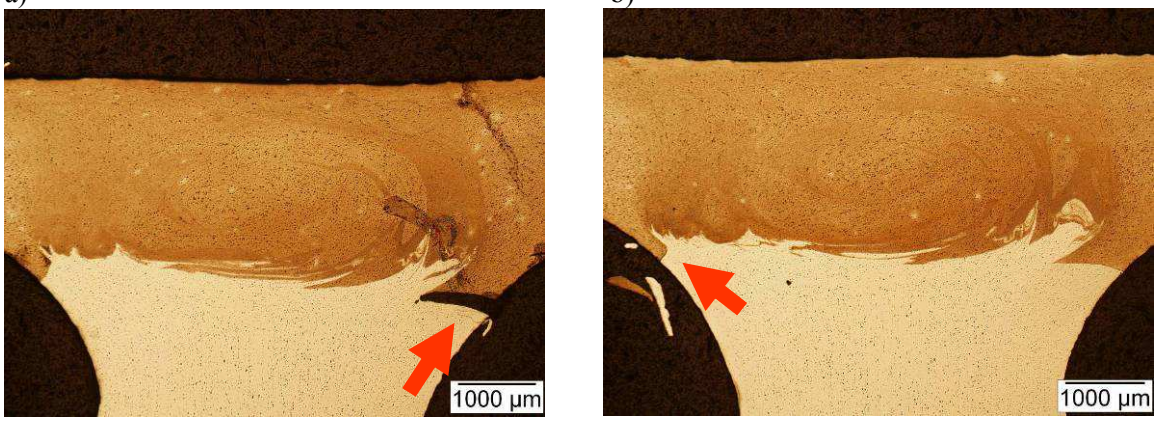

Figure 9. Metallography of a T-joint on the a) retreating side and b) advancing side.

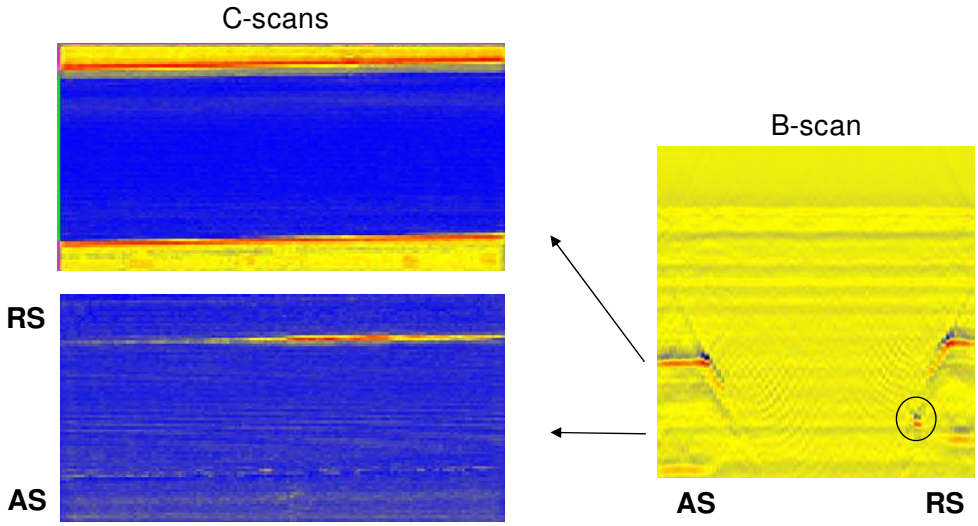

Figure 10. C-scans (left) at the depths indicated in the B-scan (right) for a T-joint sample.

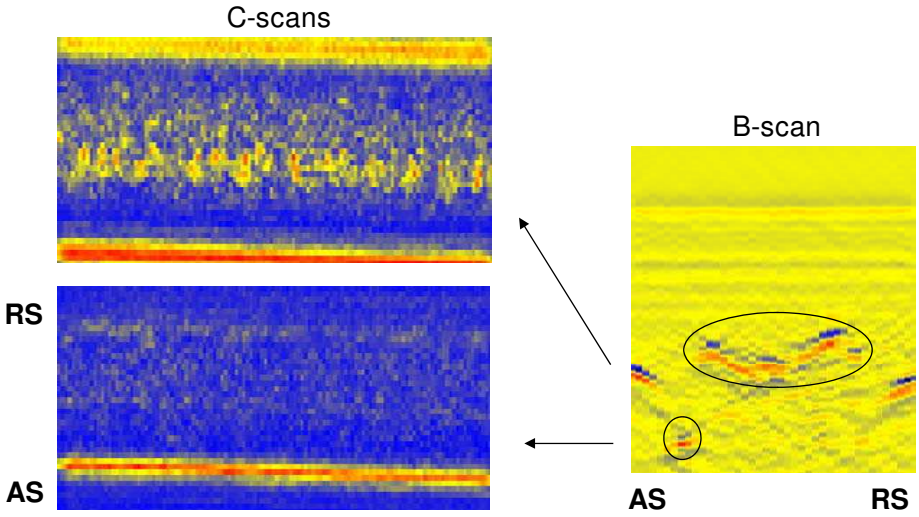

Figure 11. C-scans (left) at the depths indicated in the B-scan (right) for another T-joint sample.

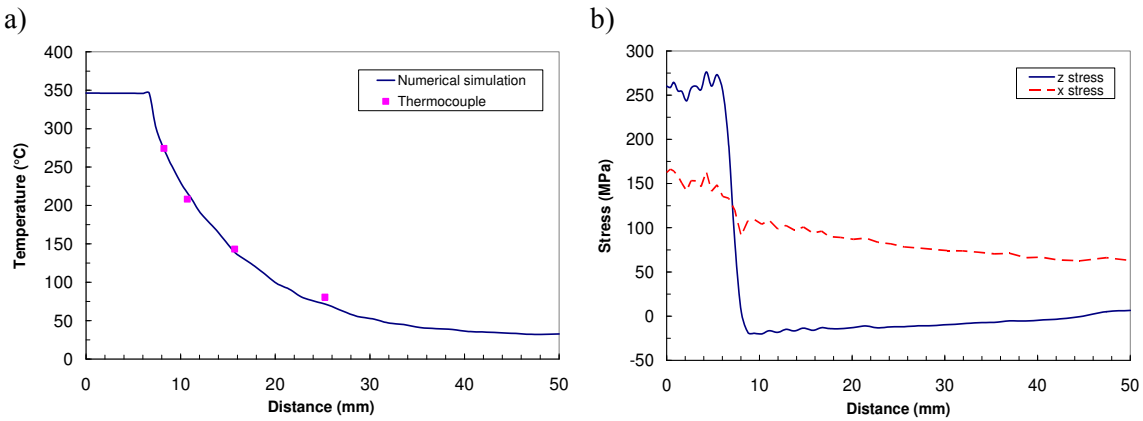

Figure 12. Calculated transverse profile across the weld line of a) maximum temperature and b) residual stresses after welding from numerical simulation of the FSW process.

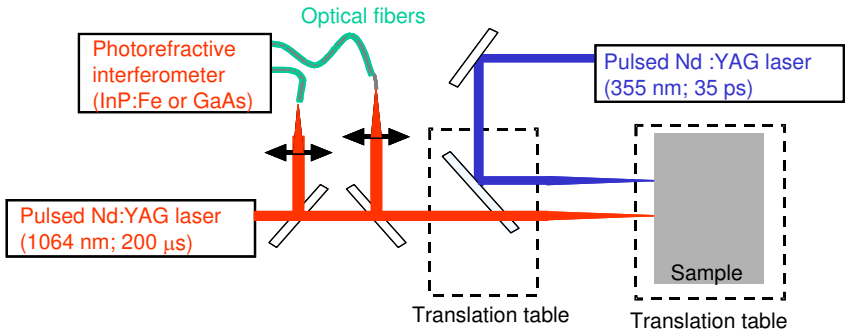

Figure 13. The laser-ultrasonic setup for residual stress measurement.

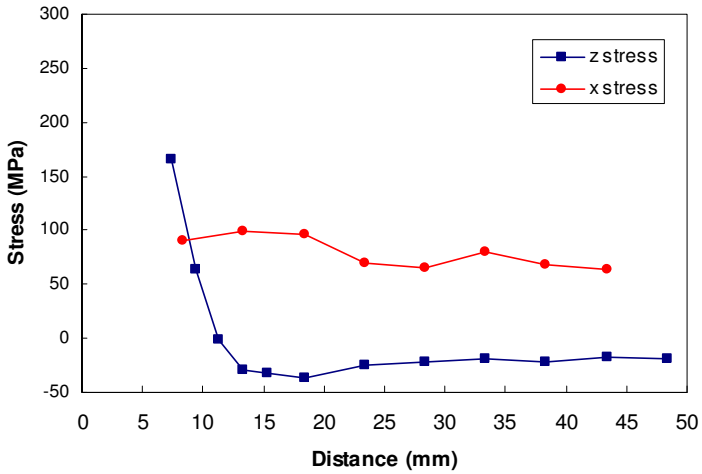

Figure 14. Transverse profile across the weld line of the z stress and x stress using laser ultrasonics.

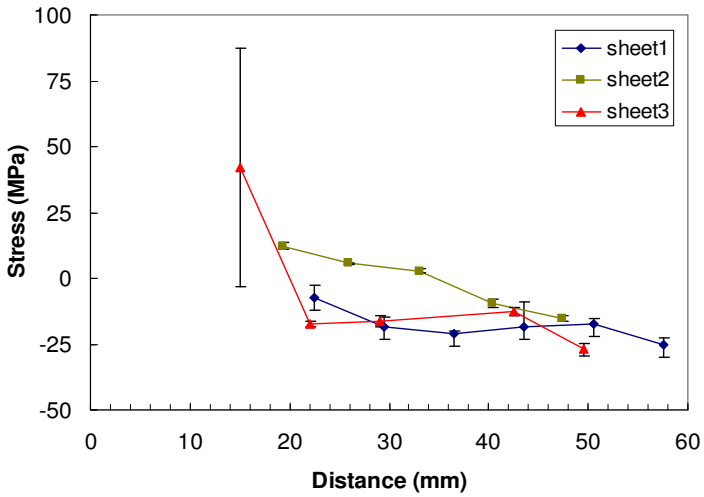

Figure 15. Transverse profile of the z stress across the weld line with error bars on three specimens using strain gauges.

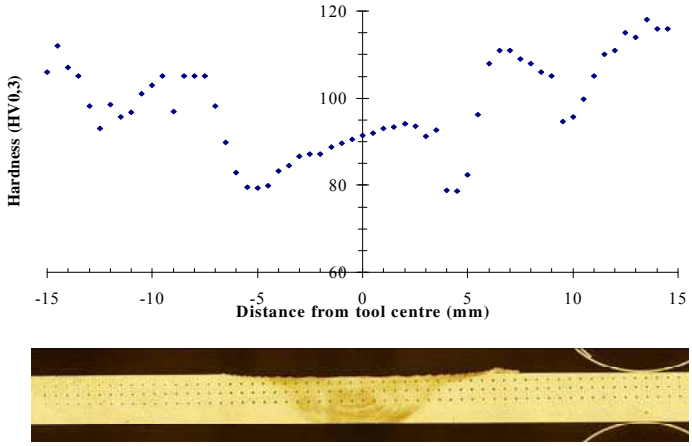

Figure 16. Cross section of the FSW weld and microhardness measurements at 1 mm from the upper surface.

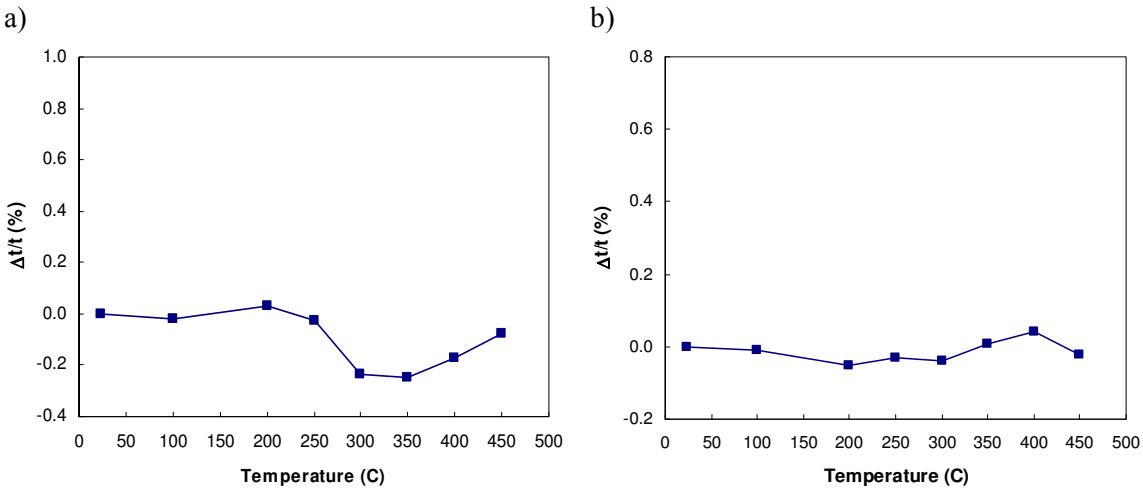

Figure 17. TOF variation on small coupons unstressed, heated at different temperatures and measured at room temperature, a) for the P-wave and b) after correction with the SAW.